A New Admittance-Type Haptic Interface for Bimanual Manipulations

Angelika Peer, *Member, IEEE*, and Martin Buss, *Member, IEEE*

Abstract—The concept of a new mobile haptic interface for bimanual manipulations in 6 DOFs is presented. The design of this mobile haptic interface is based on a modular system consisting of two components: two admittance-type haptic interfaces and a mobile platform. While the haptic interfaces cover only parts of the human arm workspace, the mobile platform extends these to arbitrarily wide remote environments. This paper mainly addresses the design and control concepts of the haptic interfaces, which are planned to be mounted on the mobile platform. The interfaces dispose of a large workspace and a high force/torque capability. A special design and control concept of the haptic interfaces makes it possible to decouple translational from rotational movements. This decoupling helps to significantly simplify the control algorithms that handle the interaction between the single components. Evaluation results concerning the Cartesian position tracking performance and the impedance display fidelity are provided. In addition, the following performance measures are analyzed: dextrous workspace, output capability, and backdrivability. In order to reduce the measurement effort, some of these measures are determined by model-based, others by measurement-based performance evaluation.

Index Terms—Inverse kinematics, mobile haptic interface, performance evaluation.

I. INTRODUCTION

HAPTIC interfaces can be described as bidirectional human–system interfaces. On the one hand, they provide the operator with force/torque information from virtual or remote environments, and on the other hand, they are used to read the operator's motion/force input. In the recent years, haptic devices have received a lot of attention: They have found their way into applications, such as medical training, rehabilitation, virtual prototyping, telesurgery, telemaintenance, as well as, micromanipulation.

However, most existing haptic interfaces are limited in their degrees of freedom (DOFs), have only a small workspace or/and a low output capability (velocity, acceleration, and force/torque capability). Thus, tasks that require 6 DOF manipulations with high interaction forces (high output capability) in extended remote or virtual environments (large workspace) are not possible.

In order to overcome these limitations, a concept for a new bimanual, mobile haptic interface has been developed. The design
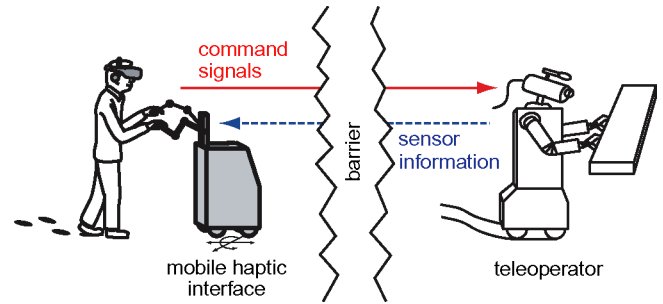
Fig. 1. Application scenario for a mobile haptic interface.

of this mobile haptic interface is based on a modular system consisting of two independently designed and driven components: two admittance-type haptic interfaces and a mobile platform. While the haptic interfaces enable manipulation tasks in a workspace of the human arm reach, the mobile platform extends this to arbitrarily wide remote environments.

Possible applications for such a system are, e.g., the control of a mobile teleoperator in a telepresence scenario (see Fig. 1) or the haptic exploration in extended virtual environments (e.g., a virtual museum).

The research presented here focuses mainly on the development of a new admittance-type haptic interface that is planned to be mounted on the mobile platform. Since the mobile platform is not able to change its position as fast as the haptic interface, the latter is designed to have a workspace adapted to the reach of a human arm. Thus, small and fast motions do not require any further position change of the mobile platform. Such a modular concept allows, on the one hand, to take into account differences in the dynamical response of the haptic interface and mobile platform, but requires, on the other hand, a haptic device with at least 6 DOFs. Furthermore, in order to be able to represent stiff environments, a haptic interface with high ouput capability and bandwidth is necessary.

This paper is organized as follows. Section II starts with a review of the state of the art in the field of stationary and mobile haptic devices. This section will be followed by a design rationale and description of the new haptic interface in Section III. Section IV presents different control algorithms that have been applied to the new device and Section V reports some evaluation results. Finally, Section VI concludes the paper and shows directions of future research.

II. STATE OF THE ART

In recent years, the interest in the development of haptic devices for telerobotic applications has dramatically increased.

A huge number of different kinds of haptic devices have been developed and partly commercialized. But, almost all of these devices are stationary devices with quite a small workspace and a moderate force level. In order to increase the workspace of such devices, usually hand-controlled input devices such as a joystick or a mouse are used [1], or some indexing technique is applied. If control by the operator's hand is not possible, as in the case of bimanual manipulation, these devices can also be substituted by a special kind of foot pedal [2], [3].

Since the operator can not move around, none of these approaches provides a proprioceptive perception of locomotion. As shown in [4], such incomplete or false proprioceptive cues result in a deterioration of the natural orientation and navigation capabilities of a human operator.

More realistic locomotion interfaces such as treadmills and tracking systems for human operator locomotion can be found in the field of virtual reality applications. These systems allow the human operator to freely move around in the remote environment, but do not provide any force feedback information. Thus, simultaneous manipulation and locomotion is not possible.

A known approach to circumvent this problem and allow simultaneous manipulation and locomotion is to use body-grounded haptic interfaces, such as exoskeletons. But, as reported in [5], working with exoskeletons is very fatiguing since the range of human arm movements is restricted and/or long-time operations are not possible because of the high weight of the system. In addition, mounting application-specific end-effectors is extremely difficult.

A much more advanced locomotion interface has been proposed in [6] and [7] and later adapted in [8]. They mounted a stationary haptic interface on a mobile platform. Since in this case, the weight of the haptic interface is fully supported by the platform, the operator fatigue can be significantly reduced. But, these systems allow only one-handed manipulation and their haptic interfaces are limited to either 3 or 4 DOFs. The first bimanual mobile haptic interface for haptic grasping in large virtual environments was presented in [9], but again haptic interfaces with only 3 DOFs were used. Moreover, due to the small workspace of the haptic interfaces, the platform has to move even for very small-size manipulations. This again means that the maximum manipulation velocity is restricted by the maximum platform velocity. A larger workspace of the haptic interfaces would also allow to perform bigger step sizes without colliding with the mobile platform.

The research presented here focuses on the development of a bimanual mobile haptic interface with the ability to manipulate in full 6 DOFs. Since the design is based on two independently controlled modules—mobile platform and haptic interfaces—haptic interfaces with at least 6 DOFs are required. In addition, a high output capability and bandwidth is necessary to represent stiff environments.

Stationary haptic interfaces that achieved a sufficient development status are mostly characterized by highly lightweight mechanical designs requiring no active force feedback control to provide a good backdrivability, e.g., the PHANToM family [10] belongs to that kind of systems. Only a few devices, e.g., the PHANToM premium, as well as, the DELTA haptic device [11]

show an improved but still moderate output capability. As the device workspace, and therefore, also the device size increases, force sensing is necessary to compensate for the increased friction and inertia. The HapticMASTER [12] is an example of such a haptic device that provides a 100-N continuous force, but is limited to 3 DOFs. The 6 DOF device Mirage F3D-35 haptic system satisfies the force requirements (peak force of about 100 N), but is limited to quite a small workspace. More advanced haptic interfaces are the Virtuose 6D40-40 with 30-N continuous force and a workspace of the human arm reach, as well as, the INCA 6D of Haption with a 40-N continuous force and an almost unlimited operational workspace. While the former is very bulky, and thus, cannot be mounted on a mobile platform, the latter seems to be only suitable for one-handed operations.

So, at the moment, no adequate haptic interface with 6 DOFs, a large workspace, and high output capability, which is furthermore mountable on a mobile platform, is available in the market. In order to fill this gap, a new bimanual admittance-type haptic interface called ViSHARD7 has been developed. Since it is mountable on a mobile platform, it is not restricted only to desktop applications but also enables bimanual manipulation tasks with high interaction forces in extended remote or virtual environments.

III. DESIGN OF NEW HAPTIC INTERFACE

A. Design Objectives

The new haptic interface should be used to perform bimanual 6 DOF teleassembling and telemanipulation tasks in large remote environments. Hereby, stiff objects such as tubes, handwheels, and metal parts of several kinds should be handled and mounted by using tools like screwdrivers and pincers. The following design objectives of this new haptic interface were chosen in accordance with this application scenario: workspace of the human arm reach free of singularities, high payload to accommodate various application-specific end-effectors as, e.g., an exoskeleton or data glove system for the human hand, high output capability, redundancy to avoid user interferences and kinematical singularities, and possible dual-arm haptic interaction with full 6-DOF capability.

To compensate for different dynamic properties of the haptic interface and mobile platform, the workspace of the haptic interfaces should be of the size of the human arm reach. On this account, manipulation tasks, which require only a small workspace, can be performed without moving the platform. Fig. 2 visualizes a typical human arm reachable workspace based on a physiological model [13]. Since most manipulations take place in front of the human operator only, this part of the workspace, which can be approximated by two intersecting hemispheres, is considered as the design criterion.

In order to also allow bimanual manipulation tasks, the workspace of the haptic interfaces must overlap. Fig. 2 clearly shows the overlapping areas of the left and right hand, which must be covered by the haptic interface.

In order to be able to extend the manipulation capabilities to a large remote environment, in addition, the following requirements must be fulfilled: First, the device must be compact and
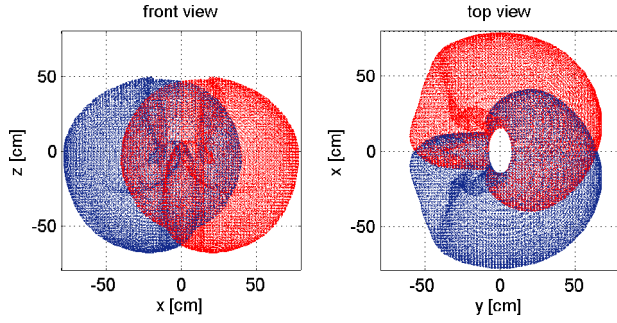
Fig. 2.   Human arm reachable workspace [13], front and top view.

Fig. 3.   Kinematic model of VISHARD7.

lightweight such that it can be mounted on a mobile platform, and second, the kinematical design must be chosen in such a way that the interaction of the mobile platform and haptic interfaces becomes feasible.

Extending the workspace of the haptic interfaces to very large-scale environments requires coupling of the haptic interfaces and mobile platform. Different optimization strategies can be used in order to position the platform in such a way that the manipulability of the haptic interfaces is maximized. In order to simplify the optimization task, a special design concept can be used to decouple translational from rotational movements of the haptic interfaces. The advantage of such a design is the possibility to compute an offline manipulability measure for the bimanual setup. This again simplifies significantly the control algorithms that manage the interaction between the mobile platform and haptic interfaces, but as a drawback, a redundant kinematical design of the haptic interfaces is necessary.

In the following, a more detailed description of the new haptic interfaces will be given.

B. Design Description

The kinematic structure of one of the haptic interfaces, called Virtual Scenario Haptic Rendering Device with 7 actuated DOFs (VISHARD7), is illustrated in Fig. 3. It shows the reference configuration with all joint angles q_i defined to be zero. The corresponding link length design is summarized in Table I. Fig. 5 shows a typical operational configuration.

The first joint has been designed as a linear axis and enables vertical motions in the z_N-direction. Joints 2 and 3 are arranged in a selective compliance assembly robot arm (SCARA) configuration and allow positioning in the x_N–y_N plane. As known in the literature, the maximum manipulability of such a two-link planar arm can be achieved for a construction with equal joint lengths. Thus, the link lengths 2 and 3 have been set to $l_2 = l_3 = 0.35$ m.

The SCARA part is in a singular configuration when links 2 and 3 are collinear. Hence, configurations near the base have to be omitted. Joint 4 is used to prevent singular configurations in the wrist formed by joints 5–7. Singularities in the wrist arise when the axes of joints 5 and 7 are collinear, which can be avoided by a rotation of joint 4. An adequate inverse kinematics algorithm guarantees singularity-free operation.
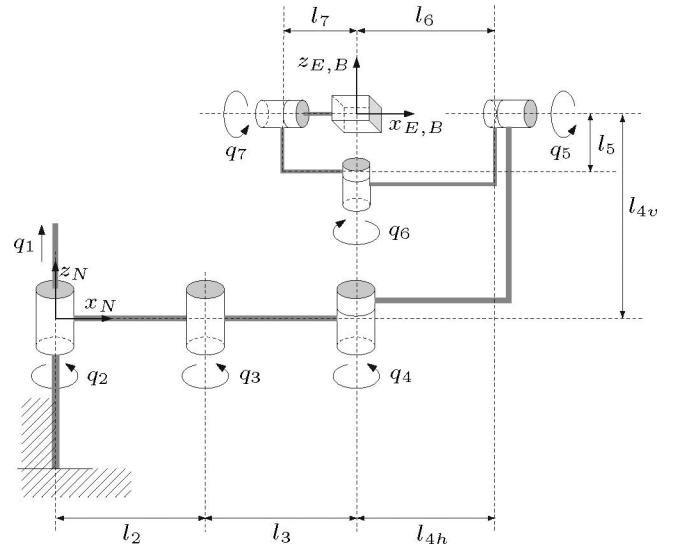
TABLE I
LINK LENGTH DESIGN OF VISHARD7

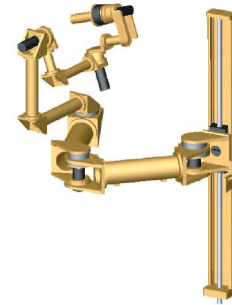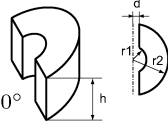| Link i	Length
l_1	0.6 m
$l_2 = l_3$	0.35 m
$l_{4h} = l_6$	0.2155 m
l_{4v}	0.3411 m
l_5	0.082 m
l_7	0.0654 m

Fig. 4.   3D-CAD model.

VISHARD7 has been designed in such a way that joints 4–7 intersect in a single point, where the angular DOFs are mechanically decoupled from the translational ones. As already mentioned in [14], such a mechanical decoupling of the angular from the translational DOFs has several advantages: The natural dynamics of the orientational DOFs is reduced and the torque capability of the rotational actuators can be chosen to match the capability of a human wrist so that no additional safety mechanisms are required. In the case of designing a mobile haptic interface consisting of two independently working components (haptic interface and mobile platform), such a construction can furthermore significantly simplify the algorithms that take care of the interaction between these two components.

Fig. 5. Bimanual mobile haptic interface.

TABLE II
SPECIFICATIONS OF VISHARD7

Property	Value
transl. workspace	$h = 0.6$ m $d = 0.1$ m $r_1 = 0.2$ m $r_2 = 0.6$ m
rot. workspace*	pitch, roll: $\pm 360°$ yaw: $\pm 60°$
peak force	vertical: 533 N horizontal: 155 N
peak torque	pitch, yaw: 11 Nm roll: 4.8 Nm
trans. velocity	vertical: 0.895 m/s horizontal: 1.1 m/s
rot. velocity*	pitch, yaw: 4.3 rad/s roll: 8.9 rad/s
trans. acceleration	vertical: 9.2 m/s^2 horizontal: 13.5 m/s^2
rot. acceleration*	pitch, yaw: 183 rad/s^2 roll: 318 rad/s^2
maximum payload**	34 kg
mass of moving parts	≈ 13 kg

*numbers refer to a device controlled by inverse function, see Sec. IV-C1.
**calculated for zero steady-state human operator input force.

The link length design guarantees a reachable workspace of almost a half-cylinder with a radius and height of 0.7 m. Thereby, possible collisions with the arm itself and the platform are considered. In contrast to this reachable workspace, the specifications of the dextrous workspace of the device are given in Table II.

The haptic interface is built by using commercially available components combined with aluminum construction elements. The actuation torque of all rotational joints is provided by dc motors coupled with harmonic drive gears offering zero backlash. The motors and gears have been selected to meet the specifications summarized in Table II. The corresponding motor, power amplifier, and gear specification data can be found in Tables III and IV. For the linear axis, an *LM Guide Actuator* of THK has been chosen, which guarantees high rigidity and high accuracy. A brushless dc motor, which carries the whole weight of all movable parts, is used to drive this linear axis. Since brushless dc motors usually have better thermal properties than comparable dc motors, this results in a more compact design. An additional brake holds the haptic interface in a fixed position when no motor currents are provided. While all dc motors of the rotational joints are supplied by Copley amplifiers configured in the torque mode, the brushless dc motor is driven by a 4QEC servo amplifier DES 70/10 of Maxon motor with sinusoidal commutation and digital current control.

In order to permit force feedback control, the device is equipped with a six-axis JR3 force–torque sensor providing a bandwidth of 8 kHz at a comparatively low noise level. The joint angles of the rotational joints are measured by digital MR encoders with a resolution of 4096 counts per revolution, resulting in a high position resolution when multiplied with the gear ratio. The position of the linear axis is measured at the drive end by using a Scancon encoder with a resolution of 30 000 counts per revolution (quadrature encoder). The combination of a slope of 10 mm/round of the linear axis and a maximum motor speed of 5370 r/min allows translational velocities of up to 0.895 m/s. The maximum payload of the linear axis is 340 N and is calculated by considering the limit of the average torque of the motor, the slope of the linear axis, and the mass of all moving parts.

Matlab/Simulink Real-Time Workshop is used to automatically generate code from Simulink models, which is then executed on an RTAI real-time operating system. All models run with a sampling rate of 1 kHz. Data acquisition is performed by using Sensoray S626 PCI-I/O boards.

IV. CONTROL

Realization of a human haptic interaction with a remote environment requires controlling of the motion–force relation between the operator and the haptic interfaces. This can be achieved by either controlling the interaction force of the device with the operator (impedance display mode) or the device motion (admittance display mode).

In order to provide effective compensation of the disturbances due to friction and the natural device dynamics, an admittance control strategy has been implemented for VISHARD7. In contrast to impedance control, which is frequently used for light and highly backdrivable devices, admittance control is particularly well suited for robots with high dynamics and nonlinearities. The high-gain inner control loop closed on motion allows for an effective elimination of the nonlinear device dynamics. Interested readers may have a look at [15] for a more detailed analysis of haptic control schemes.

The implemented admittance control is illustrated in Fig. 6. The interaction force h_h of the operator is measured by a force–torque sensor and subtracted from h_d which can be the measured interaction force of a telemanipulator with a remote environment or alternatively a force generated by a virtual environment.

The master dynamics relates the force Δh to the reference end-effector velocity $\dot{x}_r$. An algorithm for inverse kinematics resolution calculates the reference joint velocities $\dot{q}_r$. Alternatively, the mapping of the end-effector to the joint motion can be realized at the position or acceleration level. The joint angles q_r

TABLE III
SPECIFICATION OF MOTORS AND ENCODERS

Joint	Motor				Encoder		Power amplifier
#	Type	M_H^1 [Nm]	M_c^2 [Nm]	v_{max}^3 [rpm]	Type	I^4	Type
1	Maxon EC60 167132	11.8	0.747	5370	Scancon	7500	maxon DES70/10
2	Maxon RE40 148877	2.5	0.184	7580	MR-Enc. Typ L	1024	Copley 4122Z
3	Maxon RE35 273754	1.07	0.0977	7530	MR-Enc. Typ L	1024	Copley 4122Z
4	Maxon RE35 273754	1.07	0.0977	7530	MR-Enc. Typ L	1024	Copley 4122Z
5	Maxon RE30 310009	1.02	0.0882	8490	MR-Enc. Typ L	1024	Copley 4212Z
6	Maxon RE30 310009	1.02	0.0882	8490	MR-Enc. Typ L	1024	Copley 4212Z
7	Maxon RE-max29	0.268	0.0285	8660	MR-Enc. Typ ML	1024	Copley 4212Z

[1] stall torque   [2] maximum continuous torque   [3] maximum input speed   [4] impulses per turn

TABLE IV
SPECIFICATION OF GEARS

Joint#	Series-Version-Size-Ratio	M_R^1 [Nm]	M_A^2 [Nm]	v_{max}^3 [rpm]	slope [m/round]
1	THK KR45H10-D+840L	3.240 N	-	-	0.01
2	CSG-2UH-20-120	113	64	6500	-
3	HFUC-2UH-17-100	54	39	7300	-
4	CPU-M-14A-100	28	11	8500	-
5	HFUC-2A-R-11-100	11	8.9	8500	-
6	HFUC-2A-R-11-100	11	8.9	8500	-
7	HFUC-2A-R-8-100	4.8	3.3	8500	-

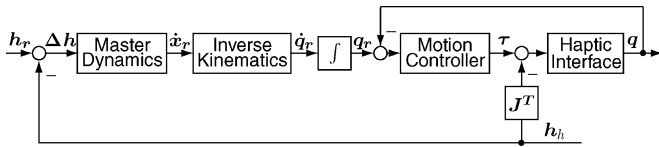[1] limit for repeated peak torque   [2] limit for average torque   [3] maximum input speed

Fig. 6.   Admittance control scheme.

are the reference inputs to a conventional position control law, e.g., independent joint controllers (IJCs) or a computed torque (CT) scheme.

In the following, the main components of this admittance control scheme will be discussed in more detail.

A. Master Dynamics

In admittance control, the minimum target mass and inertia of the haptic interface are bounded by stability: When the human operator touches the device and free space motion should be rendered, the device needs to accelerate very quickly. This again implies very high control gains, which cause potential stability problems during free space motion. Thus, in free space motion, a minimum mass and inertia necessary for stability of the master control have to be implemented. While the minimum mass is realized in the form of a double integrator

$$^N\boldsymbol{f} = \boldsymbol{M}_p\,^N\ddot{\boldsymbol{x}} \qquad (1)$$

the implementation of the minimum inertia $\boldsymbol{M}_R$ is based on the well-known Euler's dynamical equation of rotation

$$^B\boldsymbol{\mu} = \boldsymbol{M}_o\,^B\dot{\boldsymbol{\omega}} + \left(^B\boldsymbol{\omega} \times \boldsymbol{M}_o\,^B\boldsymbol{\omega}\right)\,^B\boldsymbol{\omega}. \qquad (2)$$

In this context, $_N$ and $_B$ refer to the Newtonian frame $\{N\}$ and the body coordinate frame $\{B\}$ defined in Fig. 3.

B. Motion Controller

From the huge variety of motion controllers that are known in the literature, two different approaches were implemented: IJCs, as well as, a CT scheme [16]. While the first approach neglects the nonlinear behavior of the plant and cross couplings between the linkages, the latter linearizes and decouples the system in a series of double integrators, which can be controlled independently. Thus, the IJCs are more conservative since the control gains depend hardly on the nonlinearities in the system that change according to the actual working position. In order to compensate for this effect, the CT scheme has been used.

The corresponding control laws for the two mentioned types of controllers are given with

$$\boldsymbol{\tau}_m = \boldsymbol{D}_j(\dot{\boldsymbol{q}}_r - \dot{\boldsymbol{q}}) + \boldsymbol{K}_j(\boldsymbol{q}_r - \boldsymbol{q}) \qquad (3)$$

for the IJCs and

$$\boldsymbol{\tau}_m = \tilde{\boldsymbol{M}}(\boldsymbol{q})\,\boldsymbol{u}_q + \tilde{\boldsymbol{h}}_N(\boldsymbol{q}, \dot{\boldsymbol{q}}) \qquad (4)$$

$$\boldsymbol{u}_q = \ddot{\boldsymbol{q}}_r + \boldsymbol{D}_{ct}(\dot{\boldsymbol{q}}_r - \dot{\boldsymbol{q}}) + \boldsymbol{K}_{ct}(\boldsymbol{q}_r - \boldsymbol{q}) \qquad (5)$$

for the CT scheme, where $\tilde{\boldsymbol{M}}(\boldsymbol{q})$ and $\tilde{\boldsymbol{h}}_N(\boldsymbol{q}, \dot{\boldsymbol{q}})$ denote estimates of the mass matrix, coriolis, friction, and gravity forces, and $\boldsymbol{D}_j$, $\boldsymbol{K}_j$, $\boldsymbol{D}_{ct}$, and $\boldsymbol{K}_{ct}$ are control parameters.

C. Inverse Kinematics

The inverse kinematics, the mapping of the end-effector to the joint motion, can be either realized on the position

$$\boldsymbol{q} = \boldsymbol{f}(\boldsymbol{x}) \qquad (6)$$

or on the velocity level

$$\dot{\boldsymbol{q}} = \boldsymbol{f}(\dot{\boldsymbol{x}}) \qquad (7)$$

whereby q, $\dot{q} \in \mathbf{R}^n$ are the joint angle and velocity, and x, $\dot{x} \in \mathbf{R}^m$ the end-effector position and velocity. Since for VISHARD7 $n > m$, the manipulator is redundant with respect to the end-effector task. This redundancy allows changing the internal configuration without changing the position and orientation of the end-effector. This implies that no unique solution for the inverse kinematics problem given by (6) and (7) can be derived.

To solve this problem for the haptic input device VISHARD7, two different approaches are investigated: an inverse function for the whole haptic interface as well as a so-called partitioned inverse kinematic solution, a combination of inverse function and pseudoinverse control. It should be noted that the decoupling of translational from rotational movements, which simplifies the future interaction with the mobile platform, is common for both approaches.

1) Inverse Function: A possible approach to solve the redundancy is to define a single inverse function giving the joint angles for each point of the end-effector space. A simple inverse function is defined when using the following mapping from joint angles to Cartesian positions:

$$q_1 = \left(\frac{2\pi}{0.01}\right) z \tag{8}$$

$$q_2 = \arctan 2(y, x) + \cos^{-1}\left(\frac{x^2 + y^2}{2l\sqrt{x^2 + y^2}}\right) \tag{9}$$

$$q_3 = \cos^{-1}\left(1 - \frac{x^2 + y^2}{2l^2}\right) + \pi \tag{10}$$

where (x, y, z) is the end-effector position with respect to the haptic interface base coordinate system S_N, q_i are the joint angles of the ith joint, and l is the link length of links 2 and 3. By setting joint angle 4 to $q_4 = q_{4,0} - \sum_{i=2}^{3} q_i$, a decoupling of translational and rotational motions can be achieved. It should be noted that this special inverse function implies a singular configuration at the point $x = y = 0$, which has to be omitted.

For the rotational part, an inverse kinematics solution operating at the angular velocity level has been applied. In a first step, the time derivative of the end-effector orientation (given by means of yzx-Euler-angles $[\alpha, \beta, \gamma]$) can be calculated from the angular velocity of the end-effector $^B\omega$

$$\begin{pmatrix} \dot{\alpha} \\ \dot{\beta} \\ \dot{\gamma} \end{pmatrix} = \begin{pmatrix} 0 & \dfrac{\cos\gamma}{\cos\beta} & -\dfrac{\sin\gamma}{\cos\beta} \\ 0 & \sin\gamma & \cos\gamma \\ 1 & -\dfrac{\sin\beta\cos\gamma}{\cos\beta} & \dfrac{\sin\beta\sin\gamma}{\cos\beta} \end{pmatrix} {}^B\omega. \tag{11}$$

Choosing the Euler angles in such a way that they correspond to the joint angles q_5, q_6, and q_7, the inverse function for the rotational part is given by

$$q_5 = \alpha \tag{12}$$

$$q_6 = -\beta + \pi/2 \tag{13}$$

$$q_7 = \gamma. \tag{14}$$

This inverse kinematics solution has a singular configuration for $\beta = k\pi/2$ with $k \in \mathbf{N}$, which, however, can be easily avoided by introducing a joint limitation for q_6. The drawback of this measure is obvious: The available rotational workspace is restricted to $\beta \in\ ] -\pi/2 \quad \pi/2\ [$.

2) Partitioned Inverse Kinematic Solution: To overcome this drawback and to enlarge the rotational workspace of the device, a partitioned inverse kinematic solution has been implemented. This solution uses the aforementioned inverse function for translational movements, but applies a pseudoinverse control [17] for the rotational part.

Using pseudoinverse control, a solution to the inverse problem of (7), which applies the Moore–Penrose generalized inverse $J^\# = J^T \left(JJ^T\right)^{-1}$ of the Jacobian matrix, can be formulated as follows:

$$\dot{q} = J^\# \dot{x} + [I - J^\# J]\dot{q}_0. \tag{15}$$

While the first term describes the minimum norm joint velocity solution, $[I - J^\# J]\dot{q}_0$ means the homogeneous solution of (7), which projects an arbitrary joint velocity vector $\dot{q}_0$ onto the nullspace of J. The homogeneous solution can be used to improve the device performance when choosing $\dot{q}_0$ to optimize a performance criterion $H(q)$, a scalar function of the joint angles. Redundancy can then be solved by substituting $\dot{q}_0$ with $\alpha\nabla H(q)$ resulting in

$$\dot{q} = J^\# \dot{x} + [I - J^\# J]\alpha\nabla H(q) \tag{16}$$

with α the step length of the gradient.

Replacing the Moore–Penrose generalized inverse $J^\#$ by a weighted pseudoinverse

$$J^+ = W^{-1}J^T \left(JW^{-1}J^T\right)^{-1} \tag{17}$$

with W the weighing matrix, allows further to increase or penalize the influence of certain joints on the end-effector motion. This can be of interest in the case of different velocity capabilities or mass distributions among the joints.

Under all these assumptions and considering that $q_{\text{rot}}^T = \begin{bmatrix} q_4^* & q_5 & q_6 & q_7 \end{bmatrix}$ with $q_4^* = q_4 + \sum_{i=2}^{3} q_i$, (16) becomes

$$\dot{q}_{\text{rot}} = J_{\text{rot}}^+ \omega + [I - J_{\text{rot}}^+ J_{\text{rot}}]\alpha_{\text{rot}}\nabla H_{\text{rot}} \tag{18}$$

where ω is the rotational Cartesian velocity command and $J_{\text{rot}} \in \mathbf{R}^{3\times4}$ the Jacobian relating q_{rot} to ω.

In order to avoid singularities, one of the manipulability indices $m = m(J)$ reported in [14] can be chosen as a performance criterion. However, the best results could be achieved with the following rather simple performance criterion H:

$$H = q_6^2 - \pi q_6 \qquad \text{with} \qquad \alpha < 0. \tag{19}$$

It tries to keep the sixth joint fixed to $\pi/2$, which is the position farthest away from the singular configuration.

V. PERFORMANCE EVALUATION

A. Performance Measures

Different performance measures and measurement procedures for the evaluation of haptic interfaces have been proposed

in the past (see [18]–[20]). In the following, the most common performance measures will be given. According to [19], basically two types of performance measures can be distinguished: hardware-related measures and the so-called closed-loop performance measures.

1) Hardware-Related Measures: These performance measures depend on the hardware design of the haptic interface. The most important ones are as follows:

a) dextrous workspace: number and nature (translational or rotational) of degrees of freedom, translational and rotational workspace free of singularities;

b) output capability: maximum peak and continuous force, maximum velocity, maximum acceleration, maximum payload;

c) sensorial capability: measured quantities and resolution at the human body interface

2) Closed-Loop Performance Measures: Closed-loop performance measures depend on the control of the device. The following criteria can be distinguished:

a) force precision: maximum steady-state force error at zero motion;

b) dynamic force precision: force control frequency response;

c) backdrivability: minimum apparent mass and inertia at the tip, maximum force error, impedance frequency response

d) stiffness: apparent stiffness at the human body interface;

e) smallest grating that can be rendered correctly.

In order to determine these measures, different approaches have been proposed in the past, but no general procedures have been established. The main reasons for that are the high dependency of evaluation results on the operating point and the behavior of the human operator, which is part of the system. In order to get reproducable measurement conditions, the human operator has to be replaced by a machine, which simulates the human grasping behavior. But, in the literature, still no clear design specification for such a system can be found.

Instead of specifying the presented measures only for one special operating point as is common in the literature, [18] suggests to specify best and worst case figures over the entire workspace of the device. Since this would result in a huge number of measurements, [19] proposes to obtain some of the performance measures by a model-based performance evaluation. In this paper, some of the performance measures will be obtained by model-based, others by measurement-based performance evaluation.

B. Evaluation Results

In the following sections, the evaluation results will be presented. Performance measures as dextrous workspace and output capability (maximum peak and continuous force, maximum velocity, maximum acceleration, maximum payload) are obtained by model-based, the backdrivability and some mechatronic device measures by measurement-based performance evaluation. The results are based on the previously presented control algorithms, the kinematic model shown in Fig. 3, the
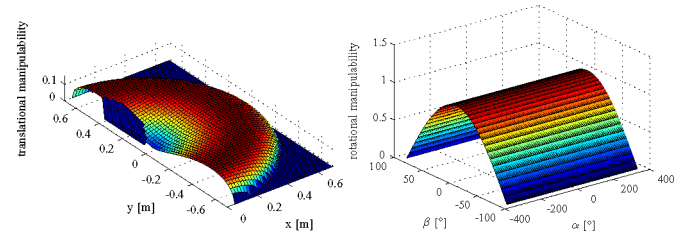

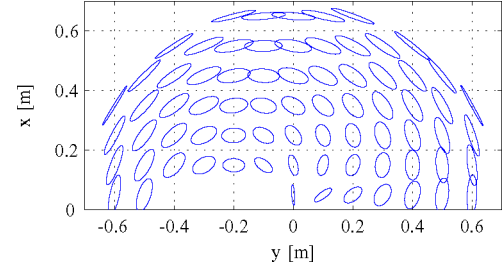Fig. 7.   Translational and rotational velocity manipulability.

Fig. 8.   Translational velocity manipulability ellipsoids.

link length design summarized in Table I, as well as, the hardware specifications of gears and motors reported in Tables III and IV.

It should be noted that considering the performance measures presented in Section V-A, difficulties arise when the system is redundant: Most of the known measurement and simulation procedures cannot be applied for such systems, because they act on the assumption that a certain Cartesian position in space can be achieved only by one joint space configuration. Thus, most of the following evaluation results have been carried out by using the inverse function, as presented in Section IV-C1.

1) Model-Based Performance Evaluation:

a) Dextrous workspace: In order to analyze the input–output transmission of the device, the velocity manipulability measure

$$m\left(\boldsymbol{q}\right) = \sqrt{\det\left(\boldsymbol{J}\left(\boldsymbol{q}\right)\boldsymbol{J}^{T}\left(\boldsymbol{q}\right)\right)} \qquad (20)$$

has been computed. The results are shown in Figs. 7 and 8. It can be clearly seen that the manipulability measure decreases in the proximity of the singularities and the boundaries of the workspace. Thus, the dextrous workspace of the device has been chosen, as stated in Table II, excluding the areas with low manipulability.

Furthermore, the form of the manipulability ellipsoids can be used as a measure for the isotropic behavior of a device. The closer the ellipsoids to the sphere, the more uniform the haptic interface can move in different directions. Fig. 8 shows the manipulability ellipsoids in different positions of the translational workspace. Considering only the dextrous workspace of the device, the ellipsoids do not differ very much in size and orientation. This again reveals that the translational motion is very uniform over the whole workspace.

b) Output capability: Typical performance measures that can be derived from model-based performance evaluation are the output and sensorial capabilities of the device. These capabilities are directly dependent on the hardware design and can be estimated using adequate kinematic and dynamic models of the device, as well as, considering the performance characteristics of single components.

In this paper, the minimum output capability of the device has been computed according to an algorithm introduced in [19], which allows to analyze the force/torque, acceleration, and velocity capabilities of the device. In contrast to other approaches based on the manipulability ellipsoid (see [21], [22]), this approach follows a different strategy. The problem to determine the minimum output capability of the device is formulated as an optimization problem. The basic idea is to find in a given working point, the direction of manipulation in which the performance of the device is worst. Extending this procedure over the whole workspace allows to determine the minimum output capability of the device.

The computation of the minimum output capability is based on the following equations, which define the velocity, force, and acceleration of the device:

$$\begin{pmatrix} \dot{x} \\ \omega \end{pmatrix} = J\dot{q} \tag{21}$$

$$h = \left(J^{-1}\right)^T \tau; \quad \dot{q} = 0 \tag{22}$$

$$\begin{pmatrix} \ddot{x} \\ \dot{\omega} \end{pmatrix} = JM^{-1}\tau; \quad \dot{q}, h = 0 \tag{23}$$

where J is the Jacobian, which relates the joint velocities $\dot{q}$ to the Cartesian velocity $\dot{x}$ and the angular velocity ω. Assuming the system is in a static case ($\dot{q} = 0$) and that the gravity and friction forces can be neglected, (22) shows the relation between the joint torques τ and the translational and rotational forces h at the end-effector. Finally, (23) denotes the relation between the joint torques τ and linear and angular accelerations $\ddot{x}$ and $\dot{\omega}$, whereby no external forces and torques are exerted on the system and M means the mass matrix of the system.

Applying the aforementioned algorithm to ViSHARD7, the following constraints have to be taken into account. Since ViSHARD7 is redundant and the presented algorithm cannot be applied to such systems, only the nonredundant case can be considered. Thus, the redundancy of the haptic interface is solved by the inverse function presented in Section IV-C1, which decouples the rotational and translational movements of the robot. This again means that the translational output capability will not be affected by the rotational one and vice versa. In the following, the obtained evaluation results will be presented.

The continuous and peak force capabilities of the haptic interface are depicted in Fig. 9. As the figure shows a constant value over the whole workspace, either joint 1 or 3 must be in saturation. While the linear axis can attain a maximum continuous/peak force of about 470/533 N, joint 3 can only provide about 27.9/154 N at the end-effector. It should be noted that the maximum forces of the second and third joints are nearly the
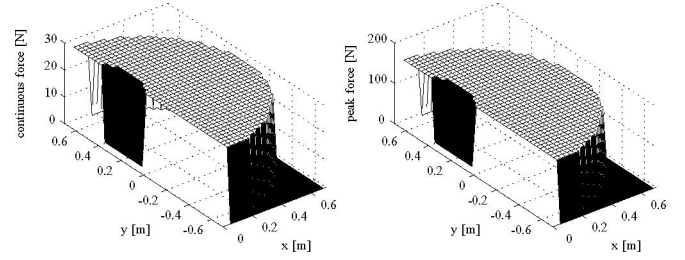

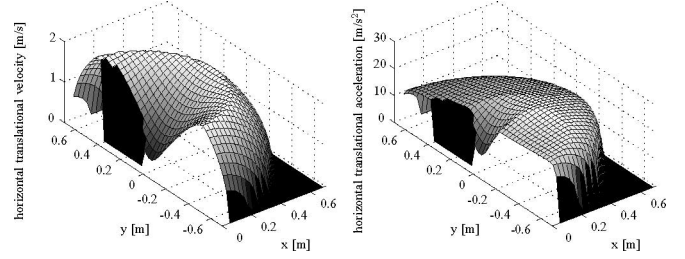Fig. 9. Horizontal translational continuous and peak force capability.

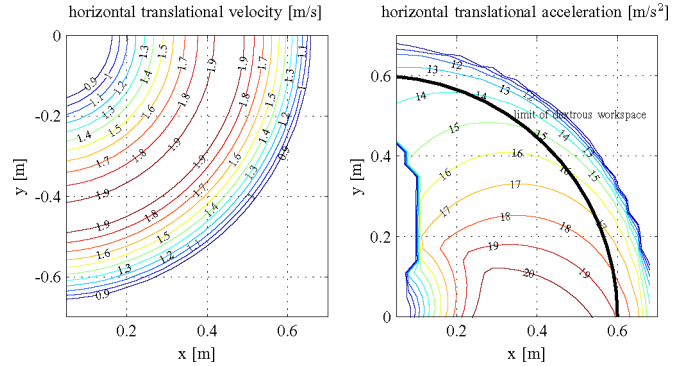Fig. 10. Maximum horizontal translational velocity and acceleration capability.

Fig. 11. Contour plot of maximum horizontal translational velocity and acceleration capability.

same, and thus, these joints represent the bottleneck of the force capability.

Fig. 10 (left) shows the horizontal translational velocity capability of the device. As supposed, the velocity performance decreases in the vicinity of the singularity near the base and at the boundaries of the reachable workspace, whereby the asymmetry around the base is a result of mechanical joint limitations. Fig. 11 (left) shows the corresponding contour plot. Considering a dextrous workspace, as stated in Table II, the maximum translational velocity for a horizontal motion results in 1.1 m/s. The maximum vertical velocity depends on the maximum velocity of the linear axis, which is given by 0.895 m/s. This indicates that the performance of the overall system could be significantly improved by decreasing the dextrous workspace and using a motor with a higher maximum motor speed for the linear axis. Unfortunately, no such motor, which meets also all
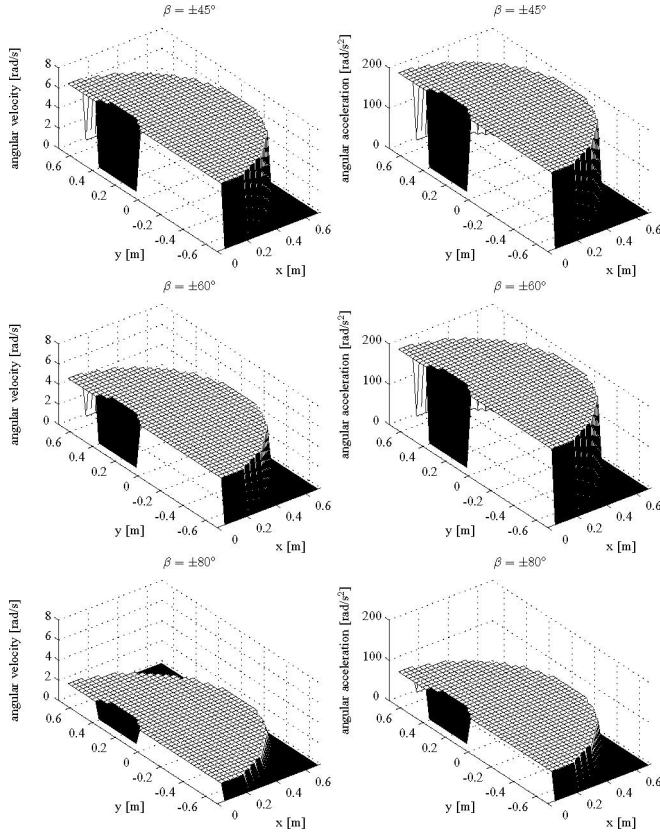
Fig. 12. Maximum horizontal rotational velocity and acceleration capability for $\beta = \pm45°, \pm60°,$ and $\pm 80°$.

other requirements as high acceleration capability, low inertia, low motor current, and high output torque, has been available in the market.

In order to determine the acceleration capability, a dynamical model of the device is necessary. Such a model is created by extracting the inertial properties from the computer-aided design (CAD) model of the device and computing the mass matrix with Autolev (see [23]). Fig. 10 (right) shows the horizontal translational acceleration capability of the system. It should be noted that the acceleration performance decreases significantly in the vicinity of singularities. Considering the dextrous workspace stated in Table II and Fig. 11 (right), the worst case horizontal acceleration capability is given by 13.5 m/s^2. The maximum vertical acceleration can be calculated by dividing the peak force of the linear axis through the mass of all moving parts. Thereby, the inertia of the axis itself (831×10^{-7} kg·m^2), the rotor of the motor (291×10^{-7} kg·m^2), and the coupling mechanism between the motor and linear axis (18×10^{-7} kg·m^2) have to be considered. This can be realized by computing an equivalent mass (45 kg) and adding it to the mass of all moving parts (13 kg). Thus, the vertical maximum acceleration is given by 9.2 m/s^2.

For the analysis of the rotational output capability of the device, the geometrical Jacobian has been used. Fig. 12 shows the rotational output capability against the Euler angles α and β, which correspond to the joint angles q_5 and q_6. Using the

inverse function presented in Section IV-C1, the haptic interface has a singularity when $\beta = \pm\pi/2$. Thus, the range of the angle β significantly influences the results on the rotational output capability. To this extent, the analysis of angular velocity and acceleration has been carried out for different ranges of the Euler angle β. Finally, the results for $\beta = 60°$ have been chosen as specifications of VISHARD7.

Finally, the limits of the torque capability of the device can be easily determined: Since the device is controlled by the inverse function described in Section IV-C1 and the Euler angles are chosen in such a way that they correspond to the joint angles q_5, q_6, and q_7, the torque capability is given by the maximum torque of the corresponding motor/gear combination (see Tables III and IV).

2) Measurement-Based Performance Evaluation:

a) Backdrivability: Since in admittance control, the inner position control loop compensates for the natural device dynamics and friction effects, the evaluation of the backdrivability can be reduced to the determination of the minimum mass M_p and inertia M_o that can be commanded without producing instability (see Section IV-A for more details). The admissible lower bound for mass and inertia is strongly dependent on the firmness of the grasp of the human operator. In order to determine numbers for this lower bound, the human operator tried to produce instability of the device by grasping it very strongly or pushing against it in different positions of the workspace. The target mass was reduced as long as no point in the workspace could be found that causes instabilities.

Depending on the position control structure and the inverse kinematics, different lower bounds for the mass and inertia can be obtained. In the experiments, simple IJCs of PD-type were compared with a more sophisticated position controller based on a CT scheme and acceleration feedforward. Concerning the inverse kinematics, two different solutions, the inverse function (see Section IV-C1) and the partitioned inverse kinematic solution (see Section IV-C2) were compared. To make the results comparable, the motion controllers (IJCs and CT scheme without acceleration feedforward) were tuned to have the same step responses. In order to do so, the following procedure has been used: After choosing appropriate control parameters for the CT scheme, the device was positioned in its working position, steps of 5 cm/° were performed for each joint, and the control parameters for the IJCs were adjusted in such a way that the step responses of both controllers became the same. The obtained control parameters are listed in Table V.

Table V finally shows also the measurement results of the backdrivability experiment. For each architecture, the control parameters as well as the mimimum mass and inertia are given. It should be noted that independently of the type of inverse kinematics, the advanced position controller with a CT scheme allows to significantly reduce the minimum mass and inertia. Among the two types of inverse kinematics, small differences in the minimum inertia can be observed. Considering that the two types of inverse kinematics move the corresponding joints in a different way, these effects can be explained by the slightly different inertias of the moving parts.

TABLE V
MINIMUM MASS AND INERTIA

Inverse kinematics	Control	Control parameters	Minimum mass and inertia
Inverse function	IJC	$\boldsymbol{K}_j = \mathrm{diag}\,(80000, 16, 14, 2, 3, 1.8, 0.5)$ $\boldsymbol{D}_j = \mathrm{diag}\,(8000, 1, 1, 0.2, 0.2, 0.1, 0.03)$	$\boldsymbol{M}_p = \mathrm{diag}\,(3.5, 3.5, 6)$ kg $\boldsymbol{M}_o = \mathrm{diag}\,(0.008, 0.04, 0.03)$ kgm^2
	CT	$\boldsymbol{K}_{ct} = \mathrm{diag}\,(400, 1000, 1000, 500, 1500, 1500, 1500)$ $\boldsymbol{D}_{ct} = \mathrm{diag}\,(40, 63.3, 63.3, 44.7, 77.5, 77.5, 77.5)$	$\boldsymbol{M}_p = \mathrm{diag}\,(2.5, 3, 3)$ kg $\boldsymbol{M}_o = \mathrm{diag}\,(0.0015, 0.02, 0.02)$ kgm^2
Partitioned inverse kinematics $\boldsymbol{W}^{\frac{1}{2}} = \mathrm{diag}\,(3, 0.2, 1, 0.1)$ $\alpha_{\mathrm{rot}} = -1$	IJC	$\boldsymbol{K}_j = \mathrm{diag}\,(80000, 16, 14, 2, 3, 1.8, 0.5)$ $\boldsymbol{D}_j = \mathrm{diag}\,(8000, 1, 1, 0.2, 0.2, 0.1, 0.03)$	$\boldsymbol{M}_p = \mathrm{diag}\,(4, 4, 6)$ kg $\boldsymbol{M}_o = \mathrm{diag}\,(0.01, 0.04, 0.03)$ kgm^2
	CT	$\boldsymbol{K}_{ct} = \mathrm{diag}\,(400, 1000, 1000, 500, 1500, 1500, 1500)$ $\boldsymbol{D}_{ct} = \mathrm{diag}\,(40, 63.3, 63.3, 44.7, 77.5, 77.5, 77.5)$	$\boldsymbol{M}_p = \mathrm{diag}\,(2.5, 3, 3)$ kg $\boldsymbol{M}_o = \mathrm{diag}\,(0.0008, 0.01, 0.01)$ kgm^2

Using pseudoinverse control, the motion behavior of the rotatory part of the display can be significantly influenced by choosing an appropriate weighing matrix. The weighing matrix, which has been used in the experiments, is given in Table V. It has been empirically found and is chosen in such a way that motions around joints 5 and 7 are relieved while motions around joint 4 are penalized. This allows to avoid really fast motions around joint 4, which may result in collisions with the mobile platform or the human operator.

b) Mechatronic Device Performance: In order to define measures of the mechatronic device performance, two experiments were performed: The first experiment evaluates the Cartesian position tracking performance and the second experiment aims at investigating the impedance display fidelity of the device.

To measure the tracking performance of the device, it was positioned in its working position and step responses for every task space coordinate were recorded. Since the velocity and acceleration capability of the device are limited (see Table II), a smooth approximation of a rectangular pulse was used

$$u = \frac{A}{2}\left(1 + \frac{\mathrm{atan}(B(t-t_1))}{\pi/2}\right) - \frac{A}{2}\left(1 + \frac{\mathrm{atan}(B(t-t_2))}{\pi/2}\right) \tag{24}$$

where $u \in \{x, y, z, \alpha, \beta, \gamma\}$ denotes a Cartesian coordinate, A and B are constants, which define amplitude and rising time of the step, and t_1, t_2 mean the moment of rising and falling edge, respectively. The parameters A and B of this function are chosen to meet the target specifications of the device: For the translational part, $A = 0.1$ m and $B = 20$, and for the rotational part, $A = 0.087$ rad and $B = 100$ have been set. In doing so, a maximum translational velocity of 0.64 m/s, a maximum translational acceleration of 8.27 m/s^2, a maximum rotational velocity of 2.77 rad/s, and a maximum rotational acceleration of 179 rad/s^2 can be achieved. Since pseudoinverse control does not allow a reference input on the position level, the derivative of the previously presented step has been used.

The experiment was carried out for two different inverse kinematics (inverse function and partitioned inverse kinematics) and two different motion controllers (IJC and CT scheme). For the motion controllers, the control parameters introduced in Table V were used.

For each controller, the translational and rotational root-mean-square (RMS) error $^p e_{\mathrm{rms}}$, $^o e_{\mathrm{rms}}$ can be computed as
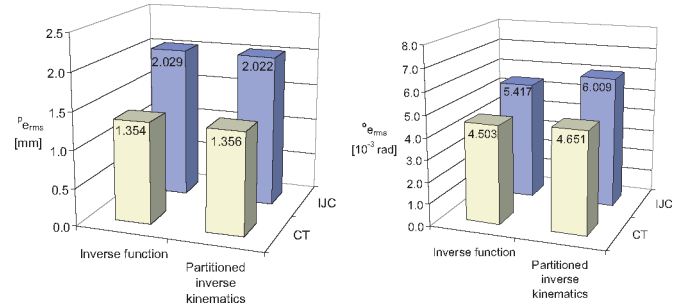

Fig. 13. Position tracking performance: translational and rotational root-mean-square tracking error.

follows:

$$^p\boldsymbol{e}_{\mathrm{rms}} = \sqrt{\frac{\sum_{i=0}^{N}|^p\boldsymbol{e}_i|^2}{N}} = \sqrt{\frac{\sum_{i=0}^{N}|\boldsymbol{x}_{ti} - \boldsymbol{x}_{mi}|^2}{N}} \tag{25}$$

$$^o\boldsymbol{e}_{\mathrm{rms}} = \sqrt{\frac{\sum_{i=0}^{N}|^o\boldsymbol{e}_i|^2}{N}} = \sqrt{\frac{\sum_{i=0}^{N}|\boldsymbol{\epsilon}_{tm}|^2}{N}} \tag{26}$$

where $\boldsymbol{x}_{ti}, \boldsymbol{x}_{mi}$ are the target and measured Cartesian positions and $\boldsymbol{\epsilon}_{tm}$ the vector part of the Quaternions $\boldsymbol{Q}_{tm} = [\eta_{tm}, \boldsymbol{\epsilon}_{tm}]$ that describes the rotation between the target and measured frame $\boldsymbol{Q}_{tm} = \boldsymbol{Q}_m^{-1} * \boldsymbol{Q}_t$ at the time-step i, N denotes the total number of time steps. Fig. 13 shows the corresponding measurement results.

As can be seen, the tracking error does not depend on the inverse kinematics, but varies with the motion controller that has been used. Using the pseudoinverese controller, in general, smaller deviations can be observed than using an independent joint controller. This is due to the smaller transient and steady-state errors of the CT-controller, which are a result of the compensated cross couplings between the linkages and gravity compensation. It should be noted that this result cannot be ascribed to differences in the stiffness of both controllers, since the experiment was carried out in the vicinity of the working position and the two joint space motion controllers were tuned to have the same joint angle step response.

The second experiment makes a comparison between the target impedance specified in the virtual environment and the rendered impedance, which can be felt by the human operator. In this experiment linear target impedances (mass–spring–damper

TABLE VI
MASS AND DAMPING FIDELITY

Motion control	Target impedance		Identified impedance		Fidelity	
	b_t [Nm/s]	m_t [kg]	b_i [Nm/s]	m_i [kg]	ζ_b	ζ_m
IJC	10	5	9.057	5.135	0.094	0.973
	20	5	19.165	5.137	1.042	0.973
	50	5	49.346	5.201	1.013	0.960
	100	5	96.154	4.944	1.038	1.011
	20	10	18.978	10.448	1.051	0.955
	20	20	18.745	21.564	1.063	0.922
	20	50	21.617	58.645	0.919	0.827
CT	10	5	7.946	5.295	1.205	0.941
	20	5	18.634	5.414	1.068	0.917
	50	5	49.012	5.814	1.020	0.837
	100	5	100.910	6.778	0.991	0.644
	20	10	17.573	10.603	1.121	0.940
	20	20	14.794	21.353	1.260	0.932
	20	50	14.336	51.715	1.283	0.966

Fig. 14. Stiffness fidelity.

systems) ranging from free space to hard contact are implemented. In order to identify the displayed impedance, force and position are measured and the rendered impedance is estimated by using the *System Identification Toolbox* of *Matlab/Simulink*. Two different identification conditions are distinguished: A free space experiment to identify the displayed mass and damping coefficients, and a contact experiment, which is used to identify the rendered stiffness of the device. It should be noted that the identification of dynamical parameters requires persistent excitation and a good signal-to-noise ratio. This means that high velocities and accelerations with different frequencies have to be applied.

In the free space experiment, different values for mass and damping coefficient are set (no stiffness), and the human operator is asked to interact with this virtual impedance by moving the end-effector with different amplitudes and frequencies. In this experiment, the force and joint velocity (calculated by differentiating the measured position) are used for estimation. In order to reduce the measurements, only results for impedances measured in the x-direction are reported. The corresponding results are shown in Table VI. Since the inverse kinematics for the translational part is unique for the *inverse function* and *partitioned inverse kinematics* solution, measurements are only taken for different kinds of motion controllers, namely the IJC and the CT scheme with and without acceleration feedforward. The same control parameters, as mentioned in Table V, were used.

The fidelity factor ζ describes the relationship between the apparent impedance and the impedance specified in the virtual environment, e.g., for the damping fidelity ζ_b the following equation holds:

$$\zeta_b = 1 - \frac{|b_t - b_i|}{b_t} \qquad (27)$$

where b_t and b_i mean the target and identified damping coefficients.

The measurement results indicate a good impedance fidelity of the device, values above 0.9 can be reached for all kind of motion controllers. In general, the IJCs show a better impedance fidelity than the controller based on a CT scheme. Finally, it should be noted that due to the high noise in the velocity signal
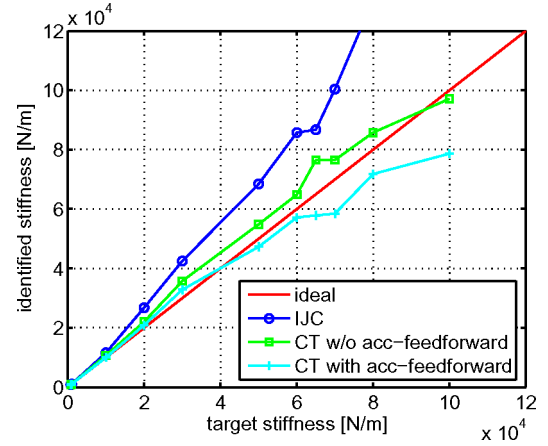
(velocity is derived by simply differentiating the position measurement) and the consequential bad signal-to-noise ratio, no identification results for free space motion (zero damping and small mass) could be obtained. In order to be able to identify such impedances, a velocity and an acceleration sensor would be necessary.

The contact experiment aims at identifying the rendered stiffness of the device. This can be realized by implementing a virtual wall with different stiffnesses and forcing the robot to push against this wall. In a steady-state condition, the apparent stiffness can then be identified as a zeroth impedance by measuring the applied force and the resulting displacement of the device. Since the human operator is not capable of providing a constant input force, the necessary force is commanded by using $\mathbf{h}_r$ (see Section IV) as the desired value. All measurements were carried out with a force of 30 N in the negative x_N-direction. Fig. 14 shows the corresponding measurement results.

In this experiment, the controller with the CT scheme shows a significantly better impedance fidelity than the IJCs with the same joint angle step response. Moreover, differences between the CT controller with and without acceleration feedforward can be observed. In general, the best result could be achieved by using a CT controller with acceleration feedforward. Allowing a maximum error of 5%, the maximum displayable stiffness for this controller is given by 65 000 N/m. Stiffnesses beyond this value cannot be displayed with an adequate precision and should be omitted.

Summarizing the control based on the CT scheme shows the best performance concerning the position tracking fidelity and the stiffness fidelity of the device. Furthermore, this controller allows to significantly reduce the minimal mass, which is necessary for stability, such that the feeling during free space motion is improved. Concerning the stiffness fidelity of the device, subjects which interacted with the device, reported also a more realistic impression of stiff walls. This might be ascribed to a better performance during transient phases, which occur, e.g., in the moment of contact with a virtual wall [24]. This, again, can be explained by an increased bandwidth of the overall system due to the feedforward term in the controller.

VI. Conclusion

The concept of a mobile haptic interface for bimanual manipulations in 6 DOFs was presented and the benefit of such a system, the ability to enable a proprioceptive perception of locomotion, is highlighted. The presented paper follows the idea of modular development. Thus, the mobile haptic interface consists of independently designed and controlled components, namely two haptic devices and a mobile platform. The design and control concepts for the haptic devices were intensively discussed. In order to simplify the interaction between haptic devices and the mobile platform, special design and inverse kinematics were chosen, which assure a decoupling of translational from rotational movements. Two types of inverse kinematics, an inverse function and a partitioned inverse kinematic solution were presented. Furthermore, two different motion controllers were implemented: IJCs and a controller based on the CT scheme.

In addition, some evaluation results were presented and the resulting specifications of the new haptic interface were determined. Hardware-related and closed-loop performance measures were distinguished, whereby the former depends only on the corresponding hardware design and the latter is connected to the implemented control architecture. In order to reduce the measurement effort, some of the performance measures were computed by model-based evaluation, while others were identified by real measurements. The following performance measures were analyzed: dextrous workspace, output capability (maximum peak and continuous force, maximum velocity, maximum acceleration, maximum payload) and backdrivability.

Finally, the mechatronic device performance was analyzed by means of the Cartesian position tracking performance and the impedance display fidelity. The evaluation results show a different position tracking performance and impedance display fidelity for the two types of motion controllers. Using motion controllers with equal joint angle step response, in general, better results could be achieved with the CT controller. It should be noted that even though the CT controller showed a smaller position tracking error, smaller minimal masses could be implemented, which results in a better free space performance. Concerning the impedance display fidelity and the position tracking performance, of course, better results could be achieved with a stiffer IJC, but this would result in a higher value for the minimal mass that can be implemented. As a consequence, the feeling of free space motion would be significantly deteriorated. The CT controller, however, seems to be able to make a compromise between the impedance display fidelity in the two extremes 1) contact and 2) free space motion, and thus, it is more appropriate for admittance-type haptic interfaces.

Future research consists in the development and implementation of a holistic control concept for the mobile haptic interface, which combines the independently controlled haptic interfaces and the mobile platform into a common control framework. A further challenge represents the integration of the new developed system in a teleoperation scenario and the evaluation of the resulting system.

References

[1] D. Lee, O. Martinez-Palafox, and M. Spong, "Bilateral teleoperation of a wheeled mobile robot over delayed communication network," in *Proc. 2006 IEEE Int. Conf. Robot. Autom.*, Orlando, FL, pp. 3298–3303.

[2] D. Caldwell, A. Wardle, O. Kocak, and M. Goodwin, "Telepresence feedback and input systems for a twin armed mobile robot," *IEEE Robot. Autom. Mag.*, vol. 3, no. 3, pp. 29–38, Sep. 1996.

[3] A. Peer, U. Unterhinninghofen, and M. Buss, "Tele-assembly in wide remote environments," presented at the 2nd Int. Workshop Human-Centered Robot. Syst., Munich, Germany, 2006.

[4] R. Darken, "Spatial orientation and wayfinding in large-scale virtual spaces ii," *Presence*, vol. 8, no. 6, pp. 3–6, 1999.

[5] A. Schiele and G. Visentin, "The ESA human arm exoskeleton for space robotics," presented at the 7th Int. Symp. Artif. Intell., Robot. Autom. Space, Nara, Japan, 2003.

[6] N. Nitzsche, U. Hanebeck, and G. Schmidt, "Design issues of mobile haptic interfaces," *J. Robot. Syst.*, vol. 20, no. 9, pp. 549–556, 2003.

[7] N. Nitzsche and G. Schmidt, "A mobile haptic interface mastering a mobile teleoperator," in *Proc. IEEE/RSJ Int. Conf. Intell. Robots Syst. (IROS)*, Sendai, Japan, 2004, pp. 3912–3917.

[8] A. Formaglio, A. Giannitrapani, M. Franzini, D. Prattichizzo, and F. Barbagli, "Performance of mobile haptic interfaces," in *Proc. 44th IEEE Eur. Control Conf. Decis. Control (CDC–ECC 2005)*, Seville, Spain, pp. 8343–8348.

[9] M. d. Pascale, A. Formaglio, and D. Prattichizzo, "A mobile platform for haptic grasping in large environments," *Virtual Real. J.*, vol. 10, pp. 11–23, 2006.

[10] T. Massie and J. Salisbury, "The PHANTOM haptic interface: A device for probing virtual objects," in *Proc. ASME Winter Annu. Meet.: Dyn. Syst. Control Div.*, New York, 1994, vol. 55, pp. 295–301.

[11] S. Grange, F. Conti, P. Rouiller, P. Helmer, and C. Baur, "Overview of the delta haptic device," presented at the Eurohaptics, England, 2001.

[12] R. Van der Linde, P. Lammertse, E. Frederiksen, and B. Ruiter, "The hapticmaster, a new high-performance haptic interface," in *Proc. Eurohaptics 2002*, Edinburgh, U.K., pp. 1–5.

[13] N. Klopcar and J. Lenarcic, "Kinematic model for determination of human arm reachable workspace," *Meccanica*, vol. 40, pp. 203–219, 2005.

[14] M. Ueberle, N. Mock, A. Peer, C. Michas, and M. Buss, "Design and control concepts of a hyper redundant haptic interface for interaction with virtual environments," presented at the IEEE/RSJ Int. Conf. Intell. Robots Syst. (IROS), Workshop on Touch Haptics, Sendai, Japan, 2004.

[15] M. Ueberle and M. Buss, "Control of kinesthetic haptic interfaces," in *Proc. IEEE/RSJ Int. Conf. Intell. Robots Syst., Workshop Touch Haptics*, 2004, pp. 147–151.

[16] P. Khosla and T. Kanade, "Real-time implementation of the computed-torque scheme," *IEEE Trans. Robot. Autom.*, vol. 5, no. 2, pp. 245–253, Apr. 1989.

[17] A. Liégeois, "c behaviour of multibody mechanisms," *IEEE Tans. Syst., Man, Cybern.*, vol. TSMC-7, no. 12, pp. 868–871, Dec. 1977.

[18] V. Hayward and O. Astley, "Performance measures for haptic interfaces," in *Proc. Robot. Res.: 7th Int. Symp.*, G. Giralt and G. Hirzinger, Eds. New York: Springer-Verlag, 1996, pp. 195–207.

[19] M. Ueberle, "Design, control, and evaluation of a family of kinesthetic haptic interfaces," Ph.D. dissertation, Technische Univ. München, Munich, Germany [Lehrstuhl für Steuerungs- und Regelungstechnik], 2006.

[20] G. Campion and V. Hayward, "Fundamental limits in the rendering of virtual haptic textures whc'05," in *Proc. First Joint Eur. Conf. Symp. Haptic Interfaces Virtual Environ. Teleoperator Syst.*, 2005, pp. 263–270.

[21] T. Yoshikawa, "Translational and rotational manipulability of robotic manipulators," in *Proc. IEEE IECON 1991*, Kobe, Japan, pp. 1170–1175.

[22] K.-S. Hong and J.-G. Kim, "Manipulability analysis of a parallel machine tool: Application to optimal link length design," *J. Robot. Syst.*, vol. 17, no. 8, pp. 403–415, 2000.

[23] T. Kane and D. Levinson. (2001). *Autolev User's Manual*, Online Dynamics, Inc., Sunnyvale, CA. [Online]. Available: www.autolev.com

[24] D. A. Lawrence, L. Y. Pao, A. M. Dougherty, M. A. Salada, and Y. Pavlou, "Rate-hardness: A new performance metric for haptic interfaces," *IEEE Trans. Robot. Autom.*, vol. 16, no. 4, pp. 357–371, Aug. 2000.

Martin Buss (S'94–M'95) was born in Germany in 1965. He received the Diploma Engineering degree in electrical engineering from the Technical University Darmstadt, Darmstadt, Germany, in 1990, and the Doctor of Engineering degree in electrical engineering from the University of Tokyo, Tokyo, Japan, in 1994.

In 2000, he finished his Habilitation in the Department of Electrical Engineering and Information Technology, Technische Universität München, Munich, Germany. During 1988, he was a Research Student at the Science University of Tokyo, Tokyo, for one year. During 1994–1995, he was a Postdoctoral Researcher in the Department of Systems Engineering, Australian National University, Canberra, Australia. From 1995 to 2000, he was a Senior Research Assistant and a Lecturer at the Institute of Automatic Control Engineering, Department of Electrical Engineering and Information Technology, Technische Universität München. From 2000 to 2003, he was appointed a Full Professor, the Head of the Control Systems Group, and the Deputy Director of the Institute of Energy and Automation Technology, Faculty IV—Electrical Engineering and Computer Science, Technical University Berlin, Berlin, Germany. Since 2003, he has been a Full Professor (Chair) and the Director of the Institute of Automatic Control Engineering, Faculty of Electrical Engineering and Information Technology, Technische Universität München. His current research interests include automatic control, mechatronics, multimodal human–system interfaces, optimization, and nonlinear and hybrid discrete–continuous systems.

Angelika Peer (M'xx) was born in Italy in 1980. She received the Diploma Engineering degree in electrical engineering and information technology in 2003 from the Technische Universität München, Munich, Germany, where she is currently working toward the Ph.D. degree at the Institute of Automatic Control Engineering.

Her current research interests include the control of redundant haptic interfaces as well as the control and evaluation of multiuser telepresence systems.